

Dissipative phase transitions in the fully-connected Ising model with p -spin interaction

Pei Wang^{1,*} and Rosario Fazio^{2,3}

¹*Department of Physics, Zhejiang Normal University, Jinhua 321004, People's Republic of China*

²*Abdus Salam ICTP, Strada Costiera 11, I-34151 Trieste, Italy*

³*Dipartimento di Fisica, Università di Napoli "Federico II", Monte S. Angelo, I-80126 Napoli, Italy[†]*

(Dated: August 25, 2020)

In this paper, we study the driven-dissipative p -spin models for $p \geq 2$. In thermodynamic limit, the equation of motion is derived by using a semiclassical approach. The long-time asymptotic states are obtained analytically, which exhibit multi-stability in some regions of the parameter space. The steady state is unique as the number of spins is finite. But the thermodynamic limit of the steady-state magnetization displays nonanalytic behavior somewhere inside the semiclassical multi-stable region. We find both the first-order and continuous dissipative phase transitions. As the number of spins increases, both the Liouvillian gap and magnetization variance vanish according to a power law at the continuous transition. At the first-order transition, the gap vanishes exponentially accompanied by a jump of magnetization in thermodynamic limit. The properties of transitions depend on the symmetry and semiclassical multistability, being qualitatively different among $p = 2$, odd p ($p \geq 3$) and even p ($p \geq 4$).

I. INTRODUCTION

Driven-dissipative systems are nowadays at the center of an intense experimental and theoretical activity. Many different experimental platforms, from cavity arrays to BEC in cavities, just to mention some important examples, have been realized leading to numerous interesting results. From the theoretical point of view, out of equilibrium phases and phase transitions have properties with no (necessary) counterpart in equilibrium. Several reviews offer a wide perspective on the field¹⁻⁴.

Many different models of driven-dissipative many-body dynamics have been scrutinized. Dissipation may radically alter the universality class of the transition itself, see e.g. Refs. [5,6]. Furthermore, the steady-state diagram may become much richer than its equilibrium counterpart. Many interesting situations have been already investigated. The phase diagram of the Bose-Hubbard model in the presence of dissipative couplings was studied in [7-10]. The Ising model on a square lattice was shown to display a first-order or second-order phase transitions, depending on the form of the Lindblad operators¹¹⁻¹³. The paramagnetic-ferromagnetic transition in the anisotropic XYZ-Heisenberg model was systematically studied by means of different approximation schemes¹⁴⁻¹⁷. Central-spin models were investigated as well, for example in [18]. In the case of single-mode bosons, the nature of transition was investigated, for example in [19]. Dissipation causes the continuous time translational symmetry to be spontaneously broken, resulting in a time-crystal²⁰⁻²³. The dissipation here stabilizes a Floquet-time-crystal phase in the central-spin model, as also confirmed by experiments on P-donor impurities in silicon²⁴. Similarly, the collective dissipation stabilizes the Floquet-time-crystal phase in the periodically-driven XY chain²⁵. Finally, the quest for determining accurate calculation of the phase structure of open many-body systems has also prompted the development of accurate numerical tools^{26,27}.

Topic of the present work is the study of the dissipative dynamics of a fully connected model. The model describes a collection of spin-1/2 with all-to-all couplings collectively coupled to an external bath. In the presence of collective coupling to the environment^{20,28} and transverse magnetic field (but no interaction in the Hamiltonian), the total magnetization displays an everlasting oscillation in the thermodynamic limit, leading to a dissipative time-crystalline phase²⁰. Phases with broken time-translational invariance in dissipative systems appear also in several different models^{21-23,29-32}, all of them essentially having long-range/collectively couplings that admit mean-field like solutions.

The extension we will consider in this work, is to look at the properties of a dissipative fully-connected spin model including the interaction among $p \geq 2$ spins. The Hamiltonian version of this model has a long history. The p -spin model was initially introduced in a spin-glass context^{33,34}, and has been under intensive investigations in the context of quantum annealing³⁵⁻⁴⁸. The dissipative dynamics of the p -spin model was explored in a recent paper⁴⁹ with Lindblad operators describing transitions between eigenstates of the Hamiltonian (hence chosen to guarantee thermalization). The system under these conditions was shown to be trapped in a long-lived metastable state, realizing the so-called Mpemba effect⁵⁰. In the present paper we consider collective Lindblad operators that lead to a non-equilibrium steady state. The resulting phase diagram is very rich and strongly depends on the value of p . Both first-order and continuous phase transitions are present, characterized by different scaling behaviours of the Liouvillian gap and local observables.

The paper is organized as follows. We introduce the model in Sec. II. Sec. III focuses on the semiclassical approach and semiclassical phase diagram. Sec. IV discusses the steady-state properties at finite- N , their scaling behavior and dissipative phase transitions. The real-time dynamics of magnetization is discussed in Sec. V. Finally, Section VI summarizes our conclusions.

II. THE MODEL

The p -spin model consists of N spins interacting through a site-independent interaction among p of them. The corresponding Hamiltonian reads

$$\hat{H} = -\frac{J}{N^{p-1}} \sum_{j_1, j_2, \dots, j_p=1}^N \hat{\sigma}_{j_1}^x \hat{\sigma}_{j_2}^x \cdots \hat{\sigma}_{j_p}^x + h \sum_{j=1}^N \hat{\sigma}_j^z, \quad (1)$$

where $\hat{\sigma}_j^\alpha$ with $\alpha = x, y, z$ are the Pauli matrices of the j -th spin. The couplings J and h are the interaction strength and Zeeman field, respectively. We set $J = 1$ as the unit of energy throughout the paper. The zero-temperature (ground state) phase diagram of the Hamiltonian (1) shows a transition at a critical value of the field h . For $p = 2$, the quantum phase transition is second-order, it becomes first-order³⁵ for $p > 2$. The presence of the dissipative coupling radically changes the picture.

The dissipative generalization of model (1) is introduced by coupling the system to an external reservoir. The dynamics of an open system is described by a suitable Master equation, obtained after integrating out the reservoirs' degrees of freedom. Here we consider a Markovian dynamics with the evolution of the system's density matrix governed by the Lindblad equation,

$$\frac{d\hat{\rho}}{dt} = -i [\hat{H}, \hat{\rho}] + \frac{\kappa}{N} [2\hat{\sigma}^- \hat{\rho} \hat{\sigma}^+ - \{\hat{\rho}, \hat{\sigma}^+ \hat{\sigma}^-\}]. \quad (2)$$

The Lindbladian, as well as the Hamiltonian, depends on the collective operators $\hat{\sigma}^\pm = \sum_j \hat{\sigma}_j^\pm$ and $\hat{\sigma}_j^\pm = (\hat{\sigma}_j^x \pm i\hat{\sigma}_j^y)/2$. The strength of the coupling to the environment is quantified by $\kappa > 0$. In Eq. (2), the jump operator $\hat{\sigma}^-$ forces the spins to be aligned in the negative z -direction (spin-down state). The Zeeman field introduces an energy difference between the spin-up and spin-down states, while the p -spin interaction aligns the spins in the x -direction. If p is even, Eq. (2) has a Z_2 symmetry. We define the unitary transformation $\hat{U} = \prod \otimes \hat{\sigma}_j^z$ which satisfies $\hat{U}^2 = 1$. Indeed, \hat{U} is a reflection transformation, which simultaneously changes the sign of each spin's x - and y -components while keeping its z -component invariant.

The interplay between the dissipative term and the Hamiltonian dynamics leads to a non-trivial steady state. For $p = 1$ the phase diagram was studied by Iemini et al.²⁰ and Hannukainen et al.²⁸. Here we extend the analysis to a generic p .

After an initial preparation (for example in a pure state with all the spins aligned in the same direction) the system is let evolve following Eq. (2). We are interested in the steady-state (long-time) regime where the expectation values of observables are computed. In thermodynamic limit, tuning the parameters κ and h may lead to Dissipative Phase Transitions (DPTs) in the steady state. Two limits must be noticed here. One is the thermodynamic limit $N \rightarrow \infty$, the other is $t \rightarrow \infty$ (dubbed the steady-state limit). The thermodynamic

limit and the steady-state limit may not commute, i.e. $\lim_{t \rightarrow \infty} \lim_{N \rightarrow \infty} \neq \lim_{N \rightarrow \infty} \lim_{t \rightarrow \infty}$. For the problem we are interested here, by taking $N \rightarrow \infty$ first, the dynamics can be studied by the semiclassical approach, to be described in the next Section. The corresponding semiclassical steady state will be denoted as SSS, whose properties are discussed in Sec. III. On the other hand, taking $t \rightarrow \infty$ first leads to the eigenstate of Liouvillian superoperator with zero eigenvalue. The state obtained by taking $N \rightarrow \infty$ after $t \rightarrow \infty$ will be called the Liouvillian steady state (LSS), whose properties are discussed in Sec. IV.

III. SEMICLASSICAL APPROACH

We first consider the dynamics in the limit $N \rightarrow \infty$. We define the operators $\hat{s}_\alpha = \sum_i \hat{\sigma}_i^\alpha / N$, which satisfy the commutation relation $[\hat{s}_\alpha, \hat{s}_\beta] = 2i \sum_\gamma \epsilon_{\alpha\beta\gamma} \hat{s}_\gamma / N$ with $\epsilon_{\alpha\beta\gamma}$ denoting the antisymmetric tensor. The magnetization components are the expectation values, i.e. $m_\alpha = \langle \hat{s}_\alpha \rangle = \mathbf{Tr} [\hat{\rho} \hat{s}_\alpha]$. To calculate the derivative of m_α with respect to t , we substitute Eq. (2) in and notice $\langle \hat{s}_\alpha \hat{s}_\beta \rangle = \langle \hat{s}_\alpha \rangle \langle \hat{s}_\beta \rangle$ as $N \rightarrow \infty$ in which limit \hat{s}_α and \hat{s}_β are commutative²⁰. The correlation vanishes in thermodynamic limit, therefore, the equations of motion for m_α become

$$\begin{aligned} \dot{m}_x &= -2hm_y + \kappa m_x m_z, \\ \dot{m}_y &= 2p m_x^{p-1} m_z + 2hm_x + \kappa m_y m_z, \\ \dot{m}_z &= -2p m_x^{p-1} m_y - \kappa (m_x^2 + m_y^2). \end{aligned} \quad (3)$$

(m_x, m_y, m_z) satisfy a group of self-consistent equations. At $t = 0$, all the spins are supposed to be aligned in a direction with azimuthal angles (θ, ϕ) . We find the initial magnetization to be $m_x(0) = m \sin \theta \cos \phi$, $m_y(0) = m \sin \theta \sin \phi$ and $m_z(0) = m \cos \theta$, where $m = \sqrt{m_x^2 + m_y^2 + m_z^2}$ is the magnitude of magnetization.

It is easy to verify that m is a constant of motion. And Eq. (3) keeps invariant if we do the replacements $m_\alpha/m \rightarrow m_\alpha$, $m^{p-1}t \rightarrow t$, $h/m^{p-1} \rightarrow h$ and $\kappa/m^{p-2} \rightarrow \kappa$. Therefore, we only need to solve Eq. (3) at $m = 1$, and the other cases ($m \neq 1$) can be mapped into it by rescaling the parameters.

As $m = 1$, the vector (m_x, m_y, m_z) is moving on a unit sphere centered at the origin. We perform the stereographic map and map the unit sphere into the x - y plane. The map is defined as

$$\begin{aligned} x &= \frac{2m_x}{1 - m_z}, \\ y &= \frac{2m_y}{1 - m_z}, \end{aligned} \quad (4)$$

with the inverse map being

$$\begin{aligned} m_x &= \frac{4x}{4+x^2+y^2}, \\ m_y &= \frac{4y}{4+x^2+y^2}, \\ m_z &= 1 - \frac{8}{4+x^2+y^2}. \end{aligned} \quad (5)$$

After the stereographic map, the equations of motion become

$$\begin{aligned} \frac{dx}{dt} &= f(x, y) \\ &= -\kappa x - 2hy - \frac{4^{p-1}p x^p y}{(x^2+y^2+4)^{p-1}}, \\ \frac{dy}{dt} &= g(x, y) \\ &= 2hx - \kappa y + \frac{1}{2} \frac{4^{p-1}p x^{p-1} (x^2 - y^2 - 4)}{(x^2+y^2+4)^{p-1}}. \end{aligned} \quad (6)$$

The dynamics of the system in the x - y plane can be well understood by analyzing the properties of its fixed points which are defined by $f(x, y) = g(x, y) = 0$ ⁵¹. In our approach, we first solve $\dot{m}_x = \dot{m}_y = \dot{m}_z = 0$ to find the fixed points on the unit sphere and then map them into the plane. Obviously, the north pole (denoted by \mathcal{N}) and the south pole (denoted by \mathcal{S}) are fixed points. The coordinates of \mathcal{S} are $(m_x^{\mathcal{S}}, m_y^{\mathcal{S}}, m_z^{\mathcal{S}}) = (0, 0, -1)$, while those of \mathcal{N} are $(0, 0, 1)$. Besides \mathcal{N} and \mathcal{S} , there exist other fixed points which are related to the solution of algebraic equation

$$\mu(\zeta) = (1 + \tilde{\kappa}\zeta)^p - \frac{p^2}{h^2}\zeta(1-\zeta)^{p-2} = 0 \quad (7)$$

in the domain $\zeta \in [0, 1]$. Here we define $\tilde{\kappa} = \kappa^2/(4h^2)$. When Eq. (7) has no root, only \mathcal{N} and \mathcal{S} are fixed points. Otherwise, Eq. (7) has two roots denoted by ζ_1 and ζ_2 , which satisfy $0 \leq \zeta_1 \leq \zeta_2 \leq 1$. Correspondingly, there exist four additional fixed points, denoted by \mathcal{P}_{\pm} and \mathcal{Q}_{\pm} . As p is odd, the coordinates of \mathcal{P}_{\pm} are

$$\begin{aligned} m_x^{\mathcal{P}_{\pm}} &= \text{sign}(\mp h) \sqrt{(1-\zeta_1)/(1+\tilde{\kappa}\zeta_1)}, \\ m_z^{\mathcal{P}_{\pm}} &= \pm \sqrt{\zeta_1}. \end{aligned} \quad (8)$$

The coordinates of \mathcal{Q}_{\pm} are obtained by replacing ζ_1 by ζ_2 in Eq. (8). As p is even, the coordinates of \mathcal{P}_{\pm} become

$$\begin{aligned} m_x^{\mathcal{P}_{\pm}} &= \pm \sqrt{(1-\zeta_1)/(1+\tilde{\kappa}\zeta_1)}, \\ m_z^{\mathcal{P}_{\pm}} &= -\text{sign}(h) \sqrt{\zeta_1}. \end{aligned} \quad (9)$$

And the coordinates of \mathcal{Q}_{\pm} are obtained by replacing ζ_1 by ζ_2 . The m_y -coordinate is $m_y = \frac{\kappa}{2h} m_x m_z$ whether p is odd or even. Table I summarizes the coordinates of \mathcal{S} , \mathcal{P}_{+} and \mathcal{P}_{-} for different p .

After the stereographic map, \mathcal{S} is mapped into the origin with the coordinates $(x_{\mathcal{S}}, y_{\mathcal{S}}) = (0, 0)$, \mathcal{N} is mapped

into infinity, and \mathcal{P}_{\pm} and \mathcal{Q}_{\pm} are mapped into somewhere in the x - y plane. Following the qualitative theory of differential equations, we linearize Eq. (6) around each fixed point. In the vicinity of \mathcal{P}_{+} , Eq. (6) can be reexpressed as

$$\frac{d}{dt} \begin{pmatrix} \Delta x \\ \Delta y \end{pmatrix} = A_{\mathcal{P}_{+}} \begin{pmatrix} \Delta x \\ \Delta y \end{pmatrix} \quad (10)$$

with

$$A_{\mathcal{P}_{+}} = \begin{pmatrix} \left. \frac{\partial f}{\partial x} \right|_{\mathcal{P}_{+}} & \left. \frac{\partial f}{\partial y} \right|_{\mathcal{P}_{+}} \\ \left. \frac{\partial g}{\partial x} \right|_{\mathcal{P}_{+}} & \left. \frac{\partial g}{\partial y} \right|_{\mathcal{P}_{+}} \end{pmatrix}, \quad (11)$$

where $\Delta x = x - x_{\mathcal{P}_{+}}$ and $\Delta y = y - y_{\mathcal{P}_{+}}$ are the coordinates relative to \mathcal{P}_{+} . In Eq. (11), the coefficient matrix has two eigenvalues. We find them to be

$$\lambda_{\pm} = \kappa m_z \pm \sqrt{(p-1)\kappa^2 - \frac{4h^2}{m_z^2} + 4h^2(p-1)}. \quad (12)$$

Here we have expressed λ_{\pm} in terms of (m_x, m_y, m_z) , whose values are given in Eqs. (8) and (9). Surprisingly, at the fixed points \mathcal{P}_{-} or \mathcal{Q}_{\pm} , the eigenvalues of coefficient matrix have the same expression as Eq. (12).

Furthermore, in the vicinity of \mathcal{S} , Eq. (6) is linearized with the coefficient matrix being

$$A_{\mathcal{S}} = \begin{pmatrix} -\kappa & -2h \\ 2h - 4I_p & -\kappa \end{pmatrix}, \quad (13)$$

where I_p equals 1 for $p = 2$ but 0 for $p > 2$. The north pole \mathcal{N} is mapped into infinity. To analyze its properties,

		Even p	Odd p
\mathcal{P}_{+}	m_x	$\sqrt{\frac{1-\zeta_1}{1+\tilde{\kappa}\zeta_1}}$	$-\text{sign}(h) \sqrt{\frac{1-\zeta_1}{1+\tilde{\kappa}\zeta_1}}$
	m_y	$-\sqrt{\frac{\tilde{\kappa}\zeta_1(1-\zeta_1)}{1+\tilde{\kappa}\zeta_1}}$	$-\sqrt{\frac{\tilde{\kappa}\zeta_1(1-\zeta_1)}{1+\tilde{\kappa}\zeta_1}}$
	m_z	$-\text{sign}(h) \sqrt{\zeta_1}$	$\sqrt{\zeta_1}$
\mathcal{P}_{-}	m_x	$-\sqrt{\frac{1-\zeta_1}{1+\tilde{\kappa}\zeta_1}}$	$\text{sign}(h) \sqrt{\frac{1-\zeta_1}{1+\tilde{\kappa}\zeta_1}}$
	m_y	$\sqrt{\frac{\tilde{\kappa}\zeta_1(1-\zeta_1)}{1+\tilde{\kappa}\zeta_1}}$	$-\sqrt{\frac{\tilde{\kappa}\zeta_1(1-\zeta_1)}{1+\tilde{\kappa}\zeta_1}}$
	m_z	$-\text{sign}(h) \sqrt{\zeta_1}$	$-\sqrt{\zeta_1}$
\mathcal{S}	m_x	0	0
	m_y	0	0
	m_z	-1	-1

TABLE I. The magnetization components of \mathcal{P}_{+} , \mathcal{P}_{-} and \mathcal{S} for different p .

we directly linearize Eq. (3) around $(m_x^{\mathcal{N}}, m_y^{\mathcal{N}}, m_z^{\mathcal{N}}) = (0, 0, 1)$. Replacing m_z by $\sqrt{1 - m_x^2 - m_y^2}$, we find the linearized equation to be $(\dot{m}_x, \dot{m}_y)^T = A_{\mathcal{N}}(m_x, m_y)^T$, where

$$A_{\mathcal{N}} = \begin{pmatrix} \kappa & -2h \\ 2h + 4I_p & \kappa \end{pmatrix}. \quad (14)$$

The eigenvalues of $A_{\mathcal{S}}$ and $A_{\mathcal{N}}$ can be obtained easily.

The properties of a fixed point is exclusively determined by its eigenvalues (see ref. [51] for the classification of fixed points). For $p = 1$ the eigenvalues being purely imaginary indicates the existence of limit cycle and then a time-crystalline phase²⁰. For $p \geq 2$ there exists no time-crystalline phase and the system always relaxes towards a (time-independent) steady state. In current model, if the real parts of λ_+ and λ_- are both negative, the fixed point is attractive, that is a point nearby always moves towards the fixed point as t increases and finally falls into it as $t \rightarrow \infty$. Except for a set of measure-zero on the unit sphere, starting from arbitrary (m_x, m_y, m_z) , one always ends at one of the attractive fixed points in the limit $t \rightarrow \infty$.

To apply the semiclassical approach, we already take $N \rightarrow \infty$. A physical state evolves into one of the attractive fixed points if we take $t \rightarrow \infty$ after $N \rightarrow \infty$. Therefore, the attractive fixed points are indeed the SSSs. Next we check which of \mathcal{N} , \mathcal{S} , \mathcal{P}_{\pm} and \mathcal{Q}_{\pm} are attractive. We discuss the cases of $p = 2$, $p \geq 3$ being odd, and $p \geq 4$ being even, separately.

In the case $p = 2$, two eigenvalues of $A_{\mathcal{N}}$ cannot both have negative real part, therefore, \mathcal{N} is never attractive. While \mathcal{S} is attractive except for $0 \leq \kappa \leq 2$ and $B_- \leq h \leq B_+$, where

$$B_{\pm} = 1 \pm \sqrt{1 - \kappa^2/4}. \quad (15)$$

\mathcal{P}_{\pm} are attractive fixed points if and only if $0 \leq \kappa \leq 2$ and $0 \leq h \leq B_+$. But \mathcal{Q}_{\pm} are never attractive. It is easy to find the coordinates of \mathcal{P}_{\pm} to be $m_z^{\mathcal{P}_{\pm}} = -h/B_+$ and $m_x^{\mathcal{P}_{\pm}} = \pm \sqrt{\frac{B_{\pm}}{2} - \frac{2h^2}{\kappa^2} B_{\pm}}$. The m_z -coordinates of \mathcal{P}_+ and \mathcal{P}_- are the same, but their m_x -coordinates or m_y -coordinates have different signs.

The attractive fixed points (SSSs) in different regions of the κ - h half-plane are displayed in fig. 1(a), in which $B_{\pm}(\kappa)$ are plotted in red lines. Three semiclassical phases are distinguished, denoted by $\{\mathcal{S}\}$, $\{\mathcal{P}_+, \mathcal{P}_-, \mathcal{S}\}$ and $\{\mathcal{P}_+, \mathcal{P}_-\}$, respectively. For $h < 0$ or $h > B_+$, \mathcal{S} is the unique attractive point. Starting from arbitrary initial state, (m_x, m_y, m_z) always falls into the south pole in the steady limit, and all the spins are aligned in the negative z -direction. For $0 < h < B_-$, there exist three attractive points, which are \mathcal{P}_{\pm} and \mathcal{S} . It depends on the initial condition whether a residue magnetization survives in the x -direction or all the spins are aligned in the z -direction. For $B_- < h < B_+$, the attractive points are \mathcal{P}_{\pm} . The steady state always has a nonzero magnetization in the x -direction. Both the bistable and tri-stable

phases are located inside the area with $0 \leq \kappa \leq 2$ and $0 \leq h \leq 2$. Furthermore, the bistable phase has a symmetric shape with respect to $h = 1$.

For $p \geq 3$ and odd, \mathcal{S} is attractive but \mathcal{N} is not in the whole parameter space. Let us consider the polynomial $\mu(\zeta)$ defined in Eq. (7), which is a smooth function with the derivative of all orders being continuous. The function $\dot{\mu}(\zeta) = d\mu/d\zeta$ increases monotonically in the interval $[0, 1/(p-1)]$ and is definitely positive in the interval $[1/(p-1), 1]$. If $\dot{\mu} < 0$ at $\zeta = 0$, μ first decreases with ζ , reaches its minimum somewhere and then increases with ζ . If $\dot{\mu} \geq 0$ at $\zeta = 0$, μ increases monotonically with ζ in the domain $[0, 1]$. Since μ at the end points $\zeta = 0, 1$ are positive, $\mu(\zeta) = 0$ has either no root or two roots (two roots can be the same). If $\mu(\zeta)$ has roots, it must have a minimum in the domain $[0, 1]$. Suppose that the minimum is at $\zeta = \zeta_c$ with $\dot{\mu}(\zeta_c) = 0$, the two roots then satisfy $\zeta_1 \leq \zeta_c \leq \zeta_2$. For a given $\tilde{\kappa}$, $\mu(\zeta)$ is definitely positive for sufficiently large h^2 (check $\mu(\zeta)$ in the limit $h^2 \rightarrow \infty$) and decreases with h^2 at every ζ . There exists a critical value h_c^2 so that $\mu(\zeta)$ has no root for $h^2 > h_c^2$, has two same roots for $h^2 = h_c^2$, but has two different roots for $h^2 < h_c^2$. At $h^2 = h_c^2$, one must have $\mu(\zeta_c) = 0$. The two equations $\dot{\mu}(\zeta_c) = 0$ and $\mu(\zeta_c) = 0$ together determine ζ_c and h_c^2 , which read

$$\zeta_c = \frac{(p-1)(\tilde{\kappa}+1) - \sqrt{(p-1)^2(\tilde{\kappa}+1)^2 - 4\tilde{\kappa}}}{2\tilde{\kappa}}, \quad (16)$$

$$h_c^2 = \frac{p^2\zeta_c(1-\zeta_c)^{p-2}}{(1+\tilde{\kappa}\zeta_c)^p}.$$

At $h^2 = h_c^2$, the roots of $\mu(\zeta)$ are $\zeta_1 = \zeta_2 = \zeta_c$. For $h^2 < h_c^2$, the roots of $\mu(\zeta)$ satisfy $\zeta_1 < \zeta_c < \zeta_2$. Eqs. (8) and (9) tell us $(m_z^{\mathcal{P}_{\pm}})^2 = \zeta_1$ and $(m_z^{\mathcal{Q}_{\pm}})^2 = \zeta_2$. And Eq. (12) gives the eigenvalues λ_{\pm} in terms of m_z . We then express $\frac{\lambda_{\pm}}{2|h|}$ at the fixed points \mathcal{P}_{\pm} (\mathcal{Q}_{\pm}) in terms of ζ_1 (ζ_2). By using Eq. (16) and the relation $\zeta_1 < \zeta_c < \zeta_2$, we find that $\text{Re}(\lambda_{\pm})$ at \mathcal{Q}_{\pm} or \mathcal{P}_+ can never be both negative, but $\text{Re}(\lambda_{\pm})$ at \mathcal{P}_- are both negative. Therefore, \mathcal{P}_- is an attractive fixed point if and only if $h^2 < h_c^2$.

In Eq. (16), h_c^2 is expressed in terms of $\tilde{\kappa} = \kappa^2/(4h_c^2)$. For given κ , we solve Eq. (16) to obtain h_c^2 . Unfortunately, an explicit expression of h_c^2 in terms of κ is inaccessible. But it is not difficult to see that there exists a critical κ_c . For $\kappa > \kappa_c$, no h_c^2 satisfies Eq. (16). For $\kappa \leq \kappa_c$, there exists a unique $h_c > 0$ satisfying Eq. (16), which will be denoted by B from now on, or

$$B(\kappa) = \sqrt{h_c^2(\tilde{\kappa})}. \quad (17)$$

B decreases with κ , reaching zero at $\kappa = \kappa_c$.

For $-B(\kappa) \leq h \leq B(\kappa)$, both \mathcal{P}_- and \mathcal{S} are attractive points. But for $|h| > B(\kappa)$, only \mathcal{S} is the attractive point. Fig. 1(b) displays the semiclassical phase diagram at $p = 3$. The κ - h half-plane is divided into two phases, denoted by $\{\mathcal{S}\}$ and $\{\mathcal{P}_-, \mathcal{S}\}$. The h -axis and the curves

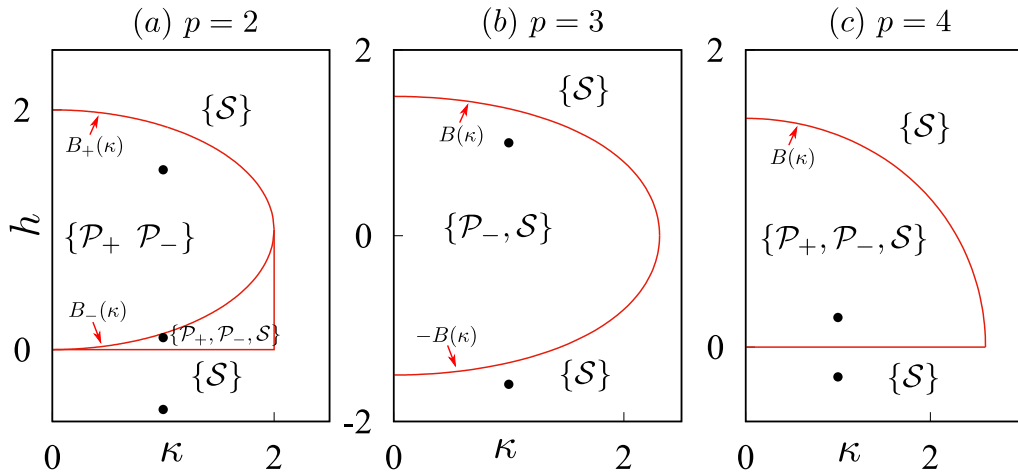


FIG. 1. (Color online) The semiclassical phase diagram in the κ - h half-plane for (a) $p = 2$, (b) $p = 3$ and (c) $p = 4$. The red solid lines are the borders between different semiclassical phases, with \mathcal{S} and \mathcal{P}_{\pm} denoting the semiclassical steady states. At the black dots, the real-time dynamics will be studied in Sec. V.

$h = \pm B(\kappa)$ surrounds the bistable phase, in which the steady state has either finite or vanishing magnetization in the x -direction, depending on the initial state. The bistable phase has a symmetric shape with respect to $h = 0$. Outside the bistable phase, all the spins are aligned in the z -direction. It is worth mentioning that the Z_2 symmetry is explicitly broken at $p = 3$. As a consequence, only \mathcal{P}_- is a SSS, but \mathcal{P}_+ is not.

For $p \geq 4$ and even, \mathcal{S} is attractive but \mathcal{N} is not in the whole parameter space. The above statements about the roots of $\mu(\zeta)$ still stand, including Eq. (16). But the coordinates of \mathcal{P}_{\pm} are different, so is the phase diagram. Fig. 1(c) shows the semiclassical phase diagram of $p = 4$. Two phases are distinguished, denoted by $\{\mathcal{S}\}$ and $\{\mathcal{P}_+, \mathcal{P}_-, \mathcal{S}\}$. For $h < 0$ or $h > B(\kappa)$, the unique attractive point is \mathcal{S} . For $0 \leq h \leq B(\kappa)$, there exist three attractive points, which are \mathcal{P}_{\pm} and \mathcal{S} . The red lines surround the tri-stable phase, in which the magnetization of SSS in the x -direction is zero or not, depending on (θ, ϕ) . The tri-stable phase only exists for $h > 0$.

IV. FINITE N

A. Method

The semiclassical approach described before cannot be used to understand the finite- N scaling behaviour. This regime is of particular importance if one would like to understand the critical properties of the Lindblad operator close to the DPTs. Moreover, on general grounds, we do expect that the multi-stability discussed in the previous Section will disappear at finite N due to the tunnelling between the different semiclassical states.

For the present problem we can use the permutation symmetry to reduce the dimension of Hilbert space from

2^N to $N + 1$. Both the Lindblad equation (2) and initial state keep invariant under the exchange of arbitrary two spins ($\hat{\sigma}_i^{\alpha} \leftrightarrow \hat{\sigma}_j^{\alpha}$). We then define the equal-weight basis (Dicke basis) as⁵²

$$|s\rangle = \frac{1}{\sqrt{C_N^{N(s+1/2)}}} \sum_{\sum_{j=1}^N \sigma_j^z = 2sN} |\sigma_1^z, \sigma_2^z, \dots, \sigma_N^z\rangle, \quad (18)$$

where $\sigma_j^z = \pm 1$ denotes the up and down states of the j th spin, respectively, and $-N \leq 2sN \leq N$ is an integer. s denotes the averaged magnetization in the z -direction, which has $N + 1$ different values, that is $s = -\frac{1}{2}, -\frac{1}{2} + \frac{1}{N}, \dots, \frac{1}{2} - \frac{1}{N}, \frac{1}{2}$. In the normalization factor, $C_N^{N(s+1/2)}$ is the binomial coefficient. The equal-weight basis $\{|s\rangle\}$ generates a $(N + 1)$ -dimensional subspace of the Hilbert space. Correspondingly, $\{|s\rangle\langle s'|\}$ generates a $(N + 1)^2$ -dimensional vector space of density matrix. The evolution of $\hat{\rho}$ is limited in this space due to the permutation symmetry.

Therefore, $\hat{\rho}$ can be expressed as $\hat{\rho} = \sum_{s,s'} \rho_{s,s'} |s\rangle\langle s'|$. From now on, we call $\rho_{s,s'}$ the density matrix. The Lindblad equation translates into

$$\begin{aligned} \frac{1}{N} \dot{\rho}_{s,s'}(t) = & [2ih(s' - s) - \kappa(f_{s'}^2 + f_s^2)] \rho_{s,s'} \\ & + 2\kappa f_{s+1/N} f_{s'+1/N} \rho_{s+1/N, s'+1/N} \\ & + iJ \left[\left(\hat{X}_s \right)^p \rho_{s,s'} - \left(\hat{X}_{s'} \right)^p \rho_{s,s'} \right], \end{aligned} \quad (19)$$

where $f_s = \sqrt{(\frac{1}{2} + s)(\frac{1}{2} - s + \frac{1}{N})}$ is a function of s . \hat{X}_s and $\hat{X}_{s'}$ are linear operators acting on the first and second arguments of $\rho_{s,s'}$, respectively. \hat{X}_s is defined by $\hat{X}_s \rho_{s,s'} = f_{s+1/N} \rho_{s+1/N, s'} + f_s \rho_{s-1/N, s'}$. Similarly, $\hat{X}_{s'}$ keeps the first argument of $\rho_{s,s'}$ invariant but changes its second argument.

Since the initial state is a pure state with all the spins aligned in the direction (θ, ϕ) , its density matrix is

$$\rho_{s,s'}(0) = \left(\cos \frac{\theta}{2} \right)^{N(1+s+s')} \left(\sin \frac{\theta}{2} \right)^{N(1-s-s')} e^{i\phi(s'-s)N} \sqrt{C_N^{N(s+1/2)} C_N^{N(s'+1/2)}}. \quad (20)$$

Given $\rho_{s,s'}(0)$, Eq. (19) can be solved numerically. Because the dimension of density matrix is $N+1$, we can easily obtain the solution for $N \leq 100$.

After obtaining $\rho_{s,s'}(t)$, we can study the time-dependent magnetization components, defined as $m_\alpha = \text{Tr}[\hat{\rho} \hat{\sigma}^\alpha] / N$. Moreover, we define the variance of magnetization in the x -direction to be $C_x = \frac{1}{N^2} \text{Tr}[\hat{\rho}(\hat{\sigma}^x)^2]$. These observables are connected to the density matrix by

$$\begin{aligned} m_x &= \sum_s \rho_{s,s-1/N} f_s + \rho_{s,s+1/N} f_{s+1/N} \\ m_y &= \sum_s i \rho_{s,s-1/N} f_s - i \rho_{s,s+1/N} f_{s+1/N} \\ m_z &= \sum_s 2s \rho_{s,s} \\ C_x &= \sum_s \rho_{s,s-2/N} f_s f_{s-1/N} + \rho_{s,s} (f_s^2 + f_{s+1/N}^2) \\ &\quad + \rho_{s,s+2/N} f_{s+1/N} f_{s+2/N}. \end{aligned} \quad (21)$$

We re-express Eq. (19) as

$$\dot{\rho}_{s,s'} = \sum_{r,r'} \mathcal{L}_{s,s';r,r'} \rho_{r,r'}, \quad (22)$$

where \mathcal{L} is the Liouvillian matrix with (s, s') denoting its row index and (r, r') denoting its column index. The dynamics of the system can be characterized by the eigenvalues and eigenvectors of \mathcal{L} . The eigenvalues of \mathcal{L} are denoted by E_n with $n = 1, 2, \dots, (N+1)^2$. E_n either is a real number, or appears in conjugate pairs. We rearrange the eigenvalues so that $\text{Re}(E_1) \geq \text{Re}(E_2) \geq \dots$. The eigenvalue with the largest real part must be 0, that is $E_1 = 0$. E_2 is the eigenvalue with the second largest real part. $\Delta = -\text{Re}E_2 > 0$ is called the Liouvillian gap, being always finite at finite N . The eigenvectors are denoted by $\rho^{(1)}, \rho^{(2)} \dots$.

The initial density matrix can be decomposed as

$$\rho_{s,s'}(0) = \rho_{s,s'}^{(1)} + \sum_{n=2}^{(N+1)^2} K_n \rho_{s,s'}^{(n)}. \quad (23)$$

Now the solution of Eq. (22) can be expressed as $\rho_{s,s'}(t) = \rho_{s,s'}^{(1)} + \sum_{n=2}^{(N+1)^2} e^{tE_n} K_n \rho_{s,s'}^{(n)}$. At finite N we always have $\text{Re}E_n < 0$ for $n \geq 2$, we then obtain

$$\lim_{t \rightarrow \infty} \rho_{s,s'}(t) = \rho_{s,s'}^{(1)}. \quad (24)$$

The steady density matrix can be directly obtained by diagonalizing \mathcal{L} without solving a differential equation. The expectation values of observables are computed by using $\rho_{s,s'}^{(1)}$ and Eq. (21). Because $\rho_{s,s'}^{(1)}$ depends on N , we denote the observables obtained in this way as $m_\alpha^{(N)}$ and $C_x^{(N)}$. Since the LSS is defined by taking $N \rightarrow \infty$ after $t \rightarrow \infty$, the observables in LSS must be expressed as

$$\begin{aligned} m_\alpha^\infty &= \lim_{N \rightarrow \infty} m_\alpha^{(N)}, \\ C_x^\infty &= \lim_{N \rightarrow \infty} C_x^{(N)}. \end{aligned} \quad (25)$$

It is worth emphasizing the different symbols that we use for LSS and SSS. The magnetizations in the former are denoted by m_α^∞ , while those in the latter are denoted by m_α^S or $m_\alpha^{P_\pm}$. Different from the SSSs, the LSS is unique for given (κ, h) and p .

At finite N , the observables ($m_\alpha^{(N)}$ and $C_x^{(N)}$) are continuous functions of h and κ . But in the limit $N \rightarrow \infty$, the observables in LSS display nonanalytic behavior somewhere inside the semiclassical multistable region. Next we discuss these nonanalytic behaviors for $p = 2$, $p = 3$ and $p = 4$ separately.

B. $p = 2$

The Lindblad equation has a reflection symmetry as p is even, at the same time, the steady state is unique at finite N . Therefore, the steady state keeps invariant under the reflection transformation \hat{U} . But \hat{U} acting on a state changes the signs of $m_x^{(N)}$ and $m_y^{(N)}$. It is possible only if $m_x^{(N)}$ and $m_y^{(N)}$ are both zero. Naturally, m_x^∞ and m_y^∞ in LSS must be zero. The steady-state magnetization has only z -component, which is apparently different from the semiclassical result. On the other hand, even if $C_x = m_x^2$ is guaranteed in semiclassical approach due to the lack of correlation, it is not the case at finite N or in the LSS. $C_x^{(N)}$ is finite while $m_x^{(N)}$ is zero. We find that m_z^∞ and C_x^∞ as a function of h display nonanalyticity for $0 < \kappa < 2$. Next we choose $\kappa = 1$ to demonstrate their properties.

From top to bottom in Fig. 2, we plot the variance in the x -direction, magnetization in the z -direction, Liouvillian gap and $\text{Im}(E_2)$ as a function of h for different N . The observables in SSSs, i.e. $m_z^S, m_z^{P_\pm}, C_x^S = (m_x^S)^2$ and $C_x^{P_\pm} = (m_x^{P_\pm})^2$, are plotted as a comparison (orange dashed and black solid lines). We mark the positions of B_- and B_+ on the h -axis. Recall that, the set of SSSs is $\{\mathcal{S}, \mathcal{P}_+, \mathcal{P}_-\}$ as $h \in [0, B_-]$, $\{\mathcal{P}_+, \mathcal{P}_-\}$ as $h \in [B_-, B_+]$, but $\{\mathcal{S}\}$ otherwise.

At finite N , $m_z^{(N)}$ and $C_x^{(N)}$ are both smooth functions of h , and Δ is finite. For $h < 0$, Δ drops linearly with increasing h . The Liouvillian gap almost vanishes at $h = A_- \approx 0.052$. On the other hand, $m_z^{(N)}(h)$ of different

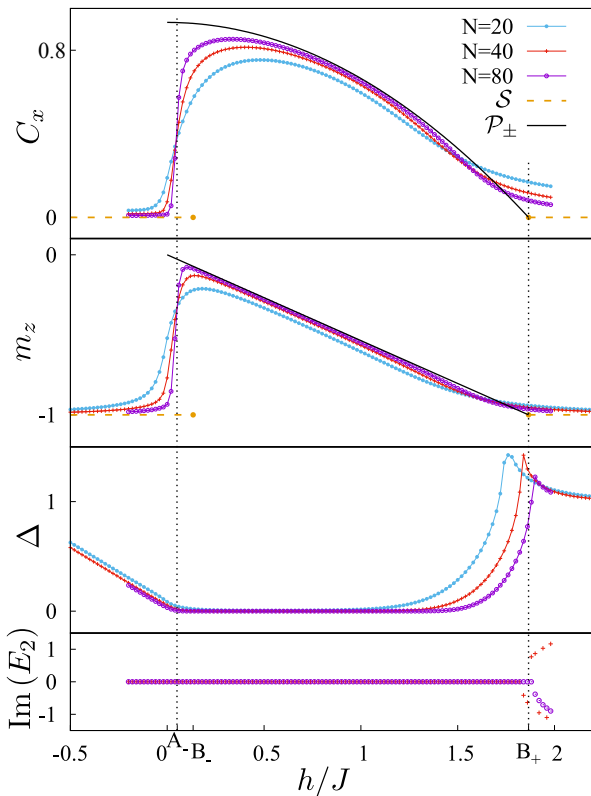


FIG. 2. (Color online) From top to bottom, we plot the variance in the x -direction, magnetization in the z -direction, Liouillian gap and $\text{Im}(E_2)$ as a function of h . Different dot types are for different N . The black solid lines are $m_z^{\mathcal{P}\pm}$ or $C_x^{\mathcal{P}\pm}$, while the orange dashed lines are $m_z^{\mathcal{S}}$ or $C_x^{\mathcal{S}}$. All the panels share the same legends. $B_- = 0.134$ is the border between tri-stable and bistable semiclassical phases. $B_+ = 1.866$ is the border between bistable and trivial phases, where a continuous transition happens. A first-order transition happens at $A_- = 0.052$. The black dotted lines indicate the location of A_- and B_+ .

N cross each other at $h = A_-$. $m_z^{(N)}$ is close to $m_z^{\mathcal{S}} = -1$ as h is much smaller than A_- , but it increases abruptly at $h = A_-$ and reaches almost $m_z^{\mathcal{P}\pm}$. Similar behavior is seen in $C_x^{(N)}$, which is close to zero for $h \ll A_-$ but increases abruptly at $h = A_-$ and reaches almost $C_x^{\mathcal{P}\pm}$. $C_x^{(N)}(h)$ of different N also cross each other at $h = A_-$, which helps us to determine the value of A_- . As N increases from 20 to 80, the change of $m_z^{(N)}$ or $C_x^{(N)}$ at $h = A_-$ becomes sharper. We guess that m_z^∞ and C_x^∞ should be discontinuous at $h = A_-$, which signals a first-order phase transition.

For $h > A_-$, the gap Δ stays small in the interval $(A_-, 1.5)$, but increases abruptly around $h = B_+$. While $m_z^{(N)}$ and $C_x^{(N)}$ drops continuously with increasing h . In the vicinity of $h = B_+$, $m_z^{(N)}$ drops back close to $m_z^{\mathcal{S}} = -1$ and $C_x^{(N)}$ drops back close to $C_x^{\mathcal{S}} = 0$. Notice that

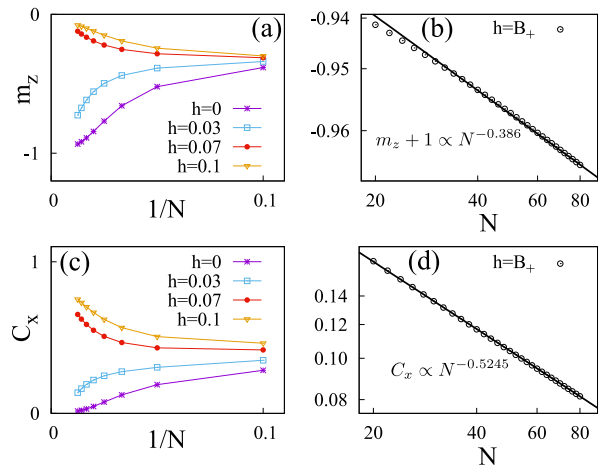


FIG. 3. (Color online) $m_z^{(N)}$ and $C_x^{(N)}$ as a function of $1/N$ are plotted in panels (a) and (c) for h in the vicinity of $A_- = 0.052$, respectively. Panels (b) and (d) plot $m_z^{(N)}$ and $C_x^{(N)}$ at $h = B_+$ with circles, respectively. And the solid lines are fits to data. Both axes of (b) or (d) are in logarithmic scale.

the fixed points \mathcal{P}_\pm meet \mathcal{S} (the south pole) at $h = B_+$ (see e.g. the orange dashed and black solid lines). For $h \in [A_-, B_+]$, as N increases from 20 to 80, $m_z^{(N)}$ ($C_x^{(N)}$) goes closer to $m_z^{\mathcal{P}\pm}$ ($C_x^{\mathcal{P}\pm}$). Especially, at $h = B_+$, $m_z^{(N)}$ or $C_x^{(N)}$ decrease towards $m_z^{\mathcal{P}\pm} = m_z^{\mathcal{S}} = -1$ or $C_x^{\mathcal{P}\pm} = C_x^{\mathcal{S}} = 0$ with increasing N , respectively. The observables are smooth functions of h at finite N so that $m_z^{(N)}$ ($C_x^{(N)}$) cannot really reach -1 (0). But it is reasonable to guess $m_z^\infty = -1$ and $C_x^\infty = 0$ for $h \geq B_+$. If this is true, $m_z^\infty(h)$ and $C_x^\infty(h)$ are nonanalytic at $h = B_+$ where a continuous phase transition happens.

In the vicinities of $h = A_-$ or $h = B_+$, we see that $\text{Im}(E_2)$ vanishes (fig. 2 the bottom panel). For large enough N (e.g. $N = 80$), $\text{Im}(E_2)$ vanishes in the whole multistable phase ($0 < h < B_+$).

To confirm the nonanalyticity of observables at $h = A_-$ and $h = B_+$, we do a scaling analysis. Figs. 3(a) and 3(c) plot $m_z^{(N)}$ and $C_x^{(N)}$ as a function of $1/N$ in the vicinity of $h = A_-$, respectively. As $1/N \rightarrow 0$ ($N \rightarrow \infty$), the observables at $h < A_-$ ($h = 0$ and $h = 0.03$) decrease, but those at $h > A_-$ ($h = 0.07$ and $h = 0.1$) increase. This bifurcation is a clear signature of m_z^∞ and C_x^∞ being discontinuous at $h = A_-$. Fig. 3(b) and fig. 3(d) plot the observables as a function of N in logarithmic scale at $h = B_+$. Both $m_z^{(N)} + 1$ and $C_x^{(N)}$ decay with increasing N , and they decay according to a power law. Their scaling behavior at large N can be approximately expressed as

$$\begin{aligned} C_x^{(N)}(B_+) &\propto N^{-0.5245}, \\ m_z^{(N)}(B_+) + 1 &\propto N^{-0.386}. \end{aligned} \quad (26)$$

In the limit $N \rightarrow \infty$, we have $C_x^\infty = 0$ and $m_z^\infty = -1$. The magnetization variance in the x -direction vanishes

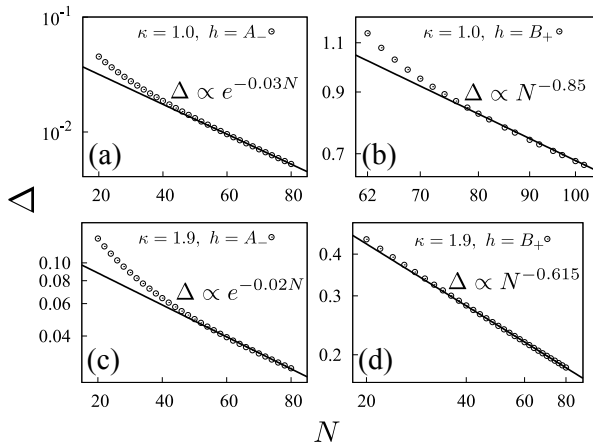


FIG. 4. (Color online) The Liouvillian gap as a function of N is plotted with circles for $\kappa = 1.0, 1.9$ and $h = A_-, B_+$. The solid lines are fits to data. Notice that the N -axis of (a) and (c) is displayed in normal scale but that of (b) and (d) is displayed in logarithmic scale.

at $h = B_+$. The scaling law (26) is reminiscent of what we see at a continuous phase transition in ground states, indicating some similarity between continuous DPT and quantum phase transition.

It was argued that the closed Liouvillian gap is a necessary condition of the nonanalyticity in LSS¹⁸. This gap is finite at finite N , and only closes in the limit $N \rightarrow \infty$. We then study how Δ changes with increasing N at $h = A_-$ and $h = B_+$. Fig. 4 plots Δ as a function of N . We not only show the gap at $\kappa = 1.0$, but also show the gap at $\kappa = 1.9$ for a comparison. The behavior of observables and gaps at $\kappa = 1.9$ is similar to that at $\kappa = 1.0$. Ref. [19] argued that the Liouvillian gap vanishes exponentially at a first-order transition. Fig. 4(a) and fig. 4(c) display Δ in logarithmic scale at $h = A_-$. For large N , Δ is approximately an exponential function of N with the exponents being $-0.03N$ and $-0.02N$ for $\kappa = 1.0$ and $\kappa = 1.9$, respectively. The exponential fit at $\kappa = 1.0$ looks better than that at $\kappa = 1.9$, possibly because the gap at $\kappa = 1.0$ is smaller. On the other hand, the Liouvillian gap vanishes according to a power law at $h = B_+$. This is observed for both $\kappa = 1.0$ and $\kappa = 1.9$ (see fig. 4(b) and fig. 4(d)). When N is large, we find $\Delta \propto N^{-\nu}$ with $\nu \approx 0.85$ ($\nu \approx 0.615$) for $\kappa = 1.0$ ($\kappa = 1.9$). The power-law vanishing of Liouvillian gap is related to the power-law vanishing of C_x^N . The continuous transition at $h = B_+$ has different properties from the first-order transition at $h = A_-$.

In short, we find a first-order DPT at $h = A_-(\kappa)$, which is characterized by the discontinuity of C_x^∞ and m_z^∞ . But at $h = B_+(\kappa)$, the DPT is continuous with C_x^∞ vanishing continuously and m_z^∞ dropping continuously to -1 . For $A_- < h < B_+$, the LSS is nontrivial, indicated by $C_x^\infty > 0$ and $m_z^\infty \neq -1$. In the nontrivial region of LSS, the magnetization in the x -direction is zero but its

variance is finite, indicating that the nontrivial state is a mixture of \mathcal{P}_+ and \mathcal{P}_- . Due to the Z_2 symmetry, there are equal probabilities for the spins to be aligned in the positive or negative x -direction. Therefore, the averaged magnetization is zero but the averaged square of magnetization is finite. We have $C_x^\infty \neq (m_x^\infty)^2$ in the nontrivial region. The correlation survives in thermodynamic limit.

We notice $0 < A_- < B_-$. The first-order DPT happens inside the tri-stable semiclassical phase in which \mathcal{P}_\pm are different from \mathcal{S} . But the continuous DPT happens at the border between the bistable phase $\{\mathcal{P}_\pm\}$ and the phase $\{\mathcal{S}\}$. At this border, the fixed points \mathcal{P}_\pm move to \mathcal{S} , explaining why C_x^∞ or m_z^∞ are continuous here.

We emphasize that our numerical method only works at small N . For N much larger than 100, it is hard to obtain the steady-state observables and Δ by diagonalizing the Liouvillian superoperator, since the dimension of density-matrix space grows as N^2 . But there exists finite-size effect at small N . Our conclusions about m_α^∞ , C_x^∞ or Δ^∞ may be seriously influenced by the finite-size effect.

C. $p = 3$

Z_2 symmetry is explicitly broken at $p = 3$. The properties of LSS are then significantly different from those at $p = 2$. Especially, the magnetizations in the x - or y -direction are not necessarily zero. The magnetization as a function of h displays nonanalyticity somewhere inside the bistable phase for κ being not very large. We choose $\kappa = 1.0$ to demonstrate the behavior of magnetization.

Fig. 5 the top panels plot $m_z^{(N)}$ and $m_x^{(N)}$ as a function of h for $N = 20, 40$ and 70 . The magnetizations of semiclassical states \mathcal{S} and \mathcal{P}_- are plotted in the same figure for comparison. \mathcal{P}_- exists only for $h \in [-B, B]$ where $\pm B$ are the borders between stable ($\{\mathcal{S}\}$) and bistable ($\{\mathcal{S}, \mathcal{P}_-\}$) phases.

$m_z^{(N)}(h)$ is an even function of h , but $m_x^{(N)}(h)$ is an odd function. This fact can be explained by using the properties of $\hat{\sigma}^z$ and $\hat{\sigma}^x$ under the reflection transformation \hat{U} . Within the interval $[-B, B]$, the curves $m_z^{(N)}(h)$ for different N cross each other at $h = -A_+, -A_-, A_-$ and A_+ . And the curves $m_x^{(N)}(h)$ cross each other at exactly the same h . The positions of $\pm A_+ \approx \pm 1.01$ and $\pm A_- \approx \pm 0.207$ are indicated by the black dotted lines in fig. 5. At $h = \pm A_+, \pm A_-$, both $m_z^{(N)}(h)$ and $m_x^{(N)}(h)$ display abrupt changes. For $h < -A_+$, $m_z^{(N)}$ is close to -1 and $m_x^{(N)}$ is close to 0, that is they are close to the coordinates of \mathcal{S} . At $h = -A_+$, $m_z^{(N)}$ increases abruptly to $m_z^{\mathcal{P}_-}$, while $m_x^{(N)}$ drops abruptly to $m_x^{\mathcal{P}_-}$. The second transition happens at $h = -A_-$, where $m_z^{(N)}$ and $m_x^{(N)}$ go back to the coordinates of \mathcal{S} . And similar transitions between \mathcal{P}_- and \mathcal{S} happen at $h = A_-$ and A_+ . As N increases from 20 to 70, the changes of $m_x^{(N)}$ and $m_z^{(N)}$ become sharper. We then expect that the change

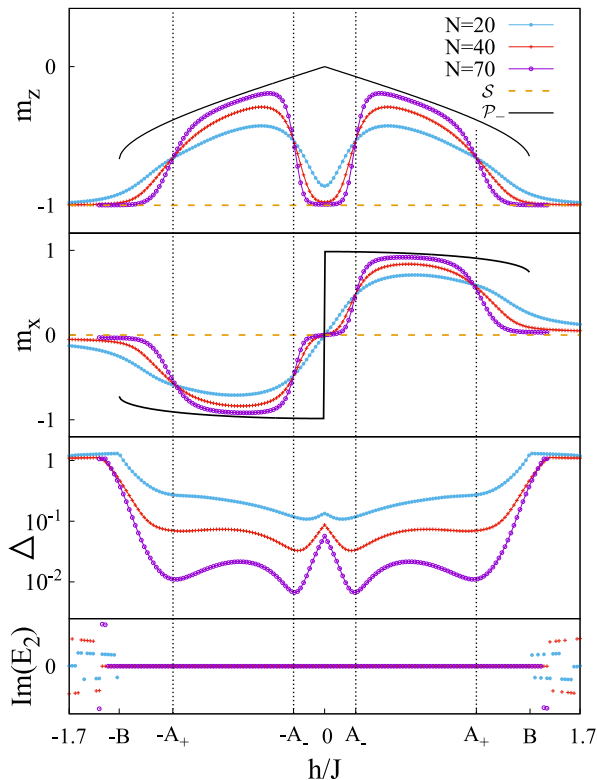


FIG. 5. (Color online) From top to bottom, we plot the magnetization in the z -direction, magnetization in the x -direction, Liouvillian gap, and imaginary part of E_2 as a function of h . Different dot colors and types are for different N . The coordinates of \mathcal{S} (orange dash) and \mathcal{P}_- (black solid) are plotted as comparison. All the panels share the same legends. $\pm B = \pm 1.367$ are the boundary of bistable phase in which \mathcal{P}_- exists. The first-order DPTs happen at $h = \pm A_+ = \pm 1.01$ and $h = \pm A_- = \pm 0.207$. The black dotted lines indicate their locations.

becomes discontinuous in thermodynamic limit.

Fig. 5 the bottom panels plot $\Delta = -\text{Re}(E_2)$ and $\text{Im}(E_2)$ as a function of h . Notice that Δ is displayed in logarithmic scale. It is clear that $\Delta(h)$ is an even function and reaches its local minimum at $h = \pm A_+, \pm A_-$. As N increases, Δ at the transition points decays towards zero, and is as small as 10^{-2} at $N = 70$. We also see that $\text{Im}(E_2)$ vanishes within the interval $[-B, B]$ for arbitrary N . In other words, $\text{Im}(E_2)$ stays zero in the vicinity of $\pm A_+$ or $\pm A_-$, similar to what happens in the case of $p = 2$.

To confirm the vanishing gap and discontinuity of observables at $h = \pm A_+$ or $\pm A_-$, we display their scaling behavior in fig. 6. The panels (a) and (c) are for $m_z^{(N)}$ and $m_x^{(N)}$ in the vicinity of $h = -A_+$, respectively. As $1/N$ goes to zero ($N \rightarrow \infty$), $m_z^{(N)}$ bends towards different directions for $h > -A_+$ ($h = -0.997, -0.977$) and for $h < -A_+$ ($h = -1.057, -1.037$), so does $m_x^{(N)}$. This indicates that m_z^∞ or m_x^∞ are discontinuous at $h = -A_+$.

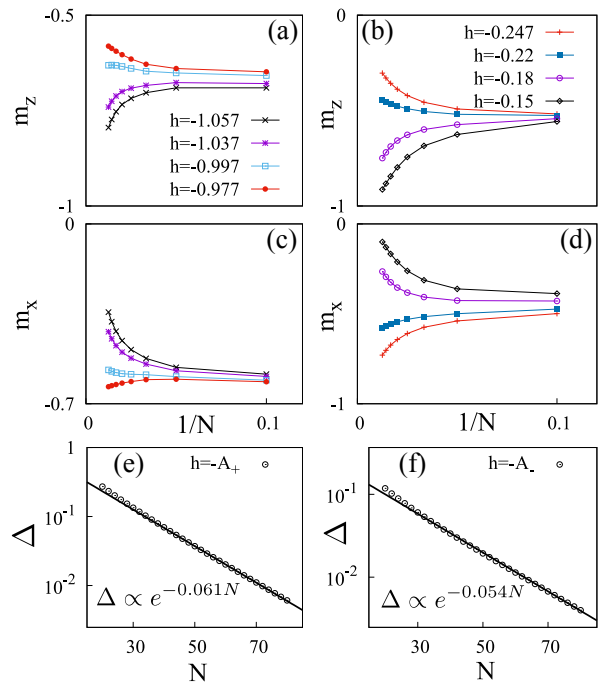


FIG. 6. (Color online) (a) $m_z^{(N)}$ vs $1/N$ in the vicinity of $h = -A_+ = -1.01$. (b) $m_z^{(N)}$ vs $1/N$ in the vicinity of $h = -A_- = -0.207$. (c) $m_x^{(N)}$ vs $1/N$ in the vicinity of $h = -A_+$. (d) $m_x^{(N)}$ vs $1/N$ in the vicinity of $h = -A_-$. (a) and (c) share the same legends. (b) and (d) share the same legends. (e) and (f) plot Δ vs N with circles at $h = -A_+$ and $-A_-$, respectively, with the solid lines being fits to data.

The panels (b) and (d) show $m_z^{(N)}$ and $m_x^{(N)}$ in the vicinity of $h = -A_-$, respectively. Similarly, the bifurcation indicates that m_z^∞ or m_x^∞ are discontinuous at $h = -A_-$. Because m_z^∞ (m_x^∞) is an even (odd) function, they must be also discontinuous at $h = A_-$ and A_+ .

Fig. 6(e) and fig. 6(f) display Δ as a function of N at $h = -A_+$ and $h = -A_-$, which perfectly fit the curves $e^{-0.061N}$ and $e^{-0.054N}$, respectively. The Liouvillian gaps vanish exponentially at the critical points, which is the feature of first-order transition.

As p is odd, the Z_2 symmetry is broken. m_x^∞ is an odd function of h , while m_z^∞ is an even function. All the DPTs are first-order, characterized by the discontinuity of m_x^∞ and m_z^∞ . The first-order DPTs happen at $h = \pm A_-$ and $\pm A_+$, which are located inside the bistable phase in which \mathcal{S} and \mathcal{P}_- are two different SSSs. LSS is one of the semiclassical states. In the regions $|h| \leq A_-(\kappa)$ or $|h| \geq A_+(\kappa)$, LSS is \mathcal{S} with spins polarized in the negative z -direction. For $A_-(\kappa) < |h| < A_+(\kappa)$, LSS is \mathcal{P}_- with finite magnetization in the x -direction. Again, we would like to emphasize that our conclusions are based on the observation at small N limited by the numerical method.

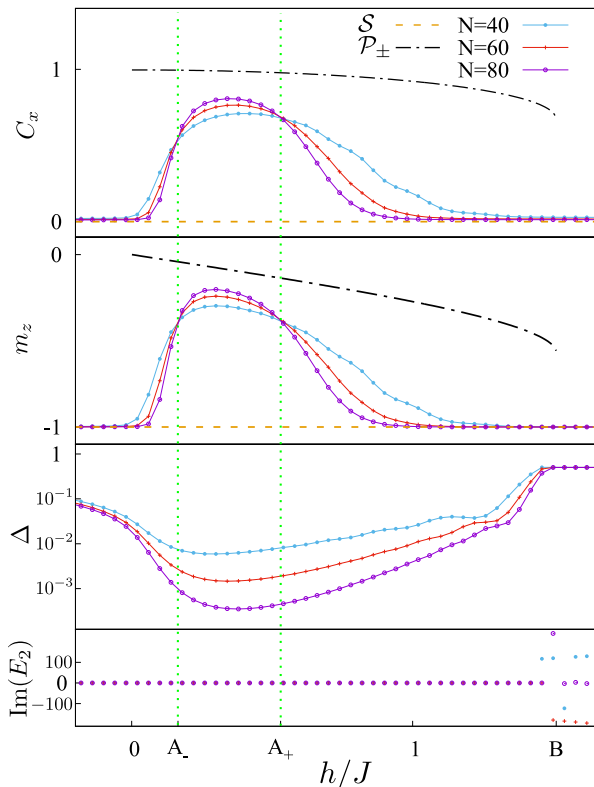


FIG. 7. From top to bottom, we plot the magnetization variance in the x -direction, magnetization in the z -direction, Liouvillian gap, and $\text{Im}(E_2)$ as a function of h . Different dot colors and types are for different N . The magnetization and variance of \mathcal{S} (orange dash) and \mathcal{P}_\pm (black dash-dotted) are plotted together as comparison. All the panels share the same legends. The system is in the tri-stable phase for $h \in [0, B]$ in which \mathcal{P}_\pm exist. The transition happens at $A_- \approx 0.165$ and $A_+ \approx 0.53$. The green dotted lines indicate the locations of A_\pm .

D. $p = 4$

The Z_2 symmetry is present at $p = 4$. The symmetry forces $m_x^{(N)} = m_y^{(N)} = 0$ and then $m_x^\infty = m_y^\infty = 0$. But the semiclassical phase diagram of $p = 4$ is qualitatively different from that of $p = 2$. m_z^∞ and C_x^∞ then show different features. They display nonanalytic behavior inside the tri-stable phase only for small enough κ (e.g. $\kappa = 0.5J$). But for large κ (e.g. $\kappa = J$), as N increases, $m_z^{(N)}$ always asymptotes -1 and $C_x^{(N)}$ asymptotes 0 for arbitrary h . Next we focus on the nonanalytic behavior at $\kappa = 0.5J$.

We plot $C_x^{(N)}$ and $m_z^{(N)}$ as a function of h for $N = 40, 60$ and 80 in fig. 7 the top panels. The observables in the SSSs, i.e. $m_z^{\mathcal{S}}$, $m_z^{\mathcal{P}_\pm}$, $C_x^{\mathcal{S}}$ and $C_x^{\mathcal{P}_\pm}$, are plotted together for comparison. Remember that \mathcal{P}_\pm exist only for $h \in [0, B]$ in which interval the system is tri-stable.

Within the interval $[0, B]$, the curves $C_x^{(N)}(h)$

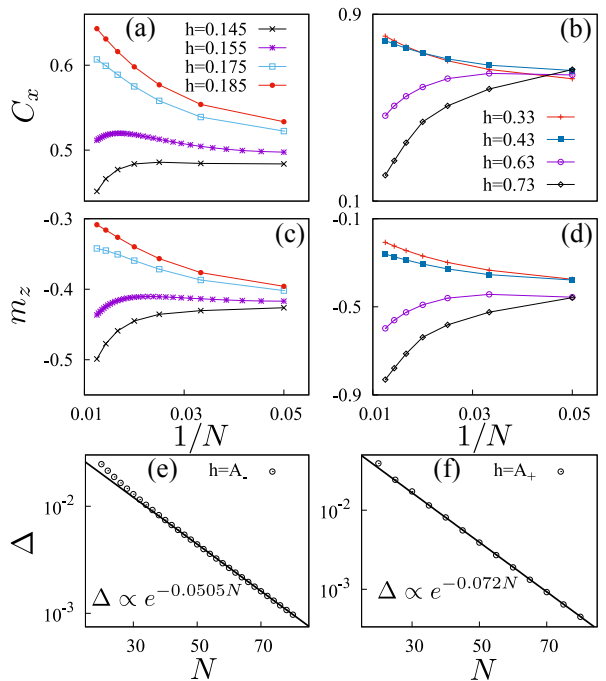


FIG. 8. (Color online) (a) $C_x^{(N)}$ vs $1/N$ in the vicinity of $h = A_- = 0.165$. (b) $C_x^{(N)}$ vs $1/N$ in the vicinity of $h = A_+ = 0.53$. (c) $m_z^{(N)}$ vs $1/N$ in the vicinity of $h = A_-$. (d) $m_z^{(N)}$ vs $1/N$ in the vicinity of $h = A_+$. (a) and (c) share the same legends. (b) and (d) share the same legends. (e) and (f) plot Δ vs N with circles at $h = A_-$ and A_+ , respectively, and the solid lines are fits to data.

($m_z^{(N)}(h)$) for different N cross each other at $h = A_- \approx 0.165$ and $A_+ \approx 0.53$. At $h = A_\pm$, $C_x^{(N)}(h)$ and $m_z^{(N)}(h)$ display abrupt changes. For $h < A_-$, $C_x^{(N)}$ ($m_z^{(N)}$) is close to 0 (-1), that is the coordinates of \mathcal{S} . At $h = A_-$, $C_x^{(N)}$ ($m_z^{(N)}$) increases abruptly towards $C_x^{\mathcal{P}_\pm}$ ($m_z^{\mathcal{P}_\pm}$). At the second critical point $h = A_+$, $C_x^{(N)}$ ($m_z^{(N)}$) drops back to 0 (-1). As N increases from 40 to 80 , the changes of $C_x^{(N)}$ and $m_z^{(N)}$ become sharper. We expect that they are discontinuous in thermodynamic limit.

Fig. 7 the bottom panels show Δ vs h and $\text{Im}(E_2)$ vs h . For $h \in [A_-, A_+]$, Δ decreases with increasing N , and is less than 10^{-3} for $N = 80$. We expect the gap to close at the transition points $h = A_\pm$ in thermodynamic limit. $\text{Im}(E_2)$ vanishes in the vicinities of A_\pm for arbitrary N , similar to what happens in the cases of $p = 2$ or $p = 3$.

We confirm the vanishing gap and discontinuity of observables at $h = A_\pm$ by doing a scaling analysis (see fig. 8). Fig. 8(a) and fig. 8(c) plot $C_x^{(N)}$ and $m_z^{(N)}$ in the vicinity of $h = A_-$, respectively. As $1/N$ goes to zero, $C_x^{(N)}$ and $m_z^{(N)}$ decrease for $h < A_-$ ($h = 0.145, 0.155$) but increase for $h > A_-$ ($h = 0.175, 0.185$), indicating the discontinuity of C_x^∞ and m_z^∞ . Panels (b) and (d) plot $C_x^{(N)}$ and $m_z^{(N)}$ in the vicinity of $h = A_+$, respec-

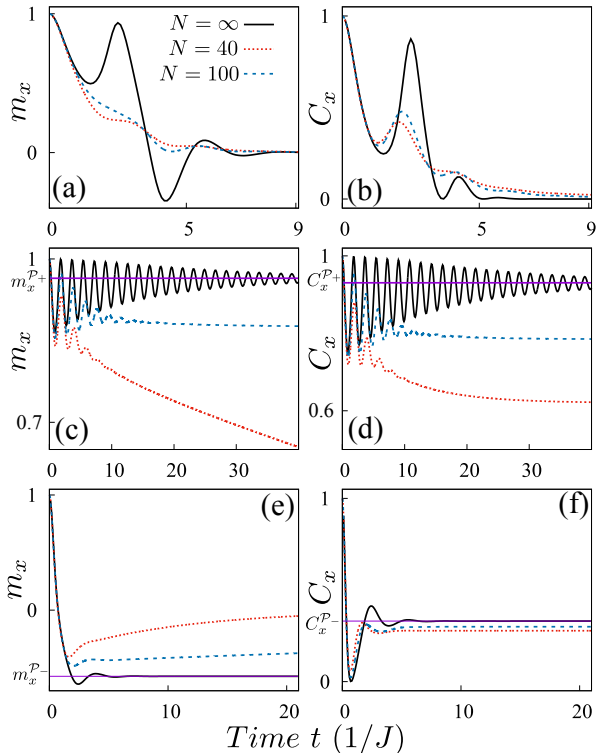


FIG. 9. (Color online) Transient dynamics of m_x and C_x at $p = 2$. Panels (a) and (b) are for $h/J = -0.5$, (c) and (d) for $h/J = 0.1$, and (e) and (f) for $h/J = 1.5$. $\kappa = J$ is fixed. The spins are initialized in the positive x -direction with $(\theta, \phi) = (\pi/2, 0)$. Different line colors and types are for different N . All the panels share the same legends. The straight purple lines are $m_x = m_x^{\mathcal{P}_\pm}$ or $C_x = C_x^{\mathcal{P}_\pm}$.

tively. Again, we see the bifurcation as $1/N \rightarrow 0$, which indicates the discontinuity of C_x^∞ and m_x^∞ . Fig. 8(e) and fig. 8(f) plot Δ as a function of N at $h = A_-$ and A_+ , respectively. The data fit the curves $e^{-0.0505N}$ at $h = A_-$ or $e^{-0.072N}$ at $h = A_+$. We conclude that the gap vanishes exponentially at the transition points.

At $p = 4$, the DPTs are first-order at $h = A_\pm(\kappa)$ which are both located inside the tri-stable semiclassical phase. For $h \leq A_-$ or $h \geq A_+$, the LSS is similar to the semiclassical state \mathcal{S} . For $A_- < h < A_+$, the LSS has vanishing magnetization but finite variance in the x -direction, which is distinguished from either \mathcal{S} or \mathcal{P}_\pm but is an equal-weight mixture of \mathcal{P}_+ and \mathcal{P}_- .

V. THE REAL-TIME DYNAMICS

In this section, we study the real-time dynamics of m_α and C_x at finite N and also in the semiclassical limit by solving Eq. (19) or (3).

Fig. 9 plots $m_x(t)$ and $C_x(t)$ in the transient regime for $p = 2$ and different values of (κ, h) whose positions in the parameter space are marked by the black dots in fig. 1(a).

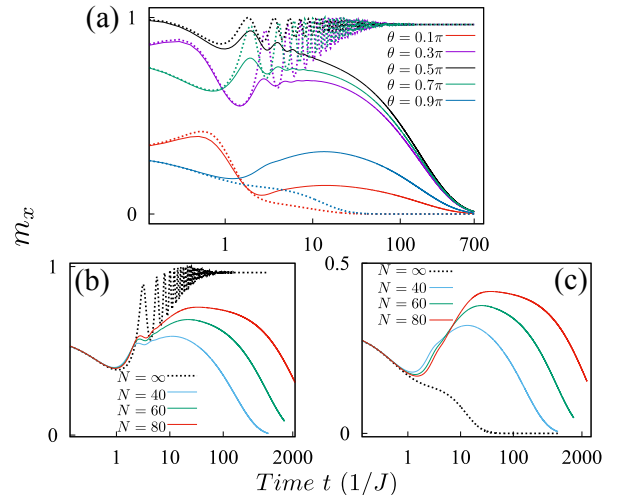


FIG. 10. (Color online) We plot $m_x(t)$ both at finite N and in semiclassical limit with different initial conditions. (a) Different line colors are for different θ . For a given θ , the solid and dotted lines are for $N = 40$ and $N \rightarrow \infty$, respectively. (b) $m_x(t)$ at different N with $\theta = 0.8\pi$. (c) $m_x(t)$ at different N with $\theta = 0.9\pi$.

The initial condition is chosen to $\theta = \pi/2$ and $\phi = 0$, i.e., the spins are along the positive- x direction. The black solid lines are $m_x(t)$ and $C_x(t)$ in the semiclassical limit. As t increases, for $h/J = -0.5, 0.1$ and 1.5 , $m_x(t)$ ($C_x(t)$) gradually approaches $m_x^{\mathcal{S}}$ ($C_x^{\mathcal{S}}$), $m_x^{\mathcal{P}_+}$ ($C_x^{\mathcal{P}_+}$) and $m_x^{\mathcal{P}_-}$ ($C_x^{\mathcal{P}_-}$), respectively. As $\kappa = J$ is fixed, $h/J = -0.5, 0.1$ and 1.5 are located in the $\{\mathcal{S}\}$ -phase, $\{\mathcal{P}_+, \mathcal{P}_-, \mathcal{S}\}$ -phase and $\{\mathcal{P}_+, \mathcal{P}_-\}$ -phase, respectively. The relaxation of $m_x(t)$ and $C_x(t)$ in the semiclassical limit coincides with the analysis in Sec. III. On the other hand, $m_x^{(N)}(t)$ or $C_x^{(N)}(t)$ at finite N deviate significantly from their semiclassical limits. Comparing the red ($N = 40$) and blue ($N = 100$) lines, we see that the blue line is closer to the black solid line. Indeed, as N goes to infinity, $m_x^{(N)}(t)$ or $C_x^{(N)}(t)$ at arbitrary finite t must converge to their semiclassical limits, respectively. For small t ($tJ < 1$), $m_x^{(N)}(t)$ and $C_x^{(N)}(t)$ converge quickly with increasing N and their values at $N = 100$ are already indistinguishable from the semiclassical limits. But as t increases, a larger N is needed for observing the convergence. For $tJ = 10$, we see a clear difference between $m_x^{(N)}(t)$ ($C_x^{(N)}(t)$) at $N = 100$ and the semiclassical limits (see fig. 9(c)-fig. 9(f)).

We choose $(\kappa, h) = (1, 0.1)$ (in the $\{\mathcal{P}_+, \mathcal{P}_-, \mathcal{S}\}$ phase) and plot $m_x(t)$ for different initial conditions at much larger time scales in fig. 10(a). We fix $\phi = 0$ and try different values of θ (initial spins are aligned in the xz -plane with positive x -component). Due to the Z_2 symmetry, $m_x^{(N)}(t)$ at finite N always decays to zero as $t \rightarrow \infty$ for whatever θ . But in the semiclassical limit $N \rightarrow \infty$, $\theta = 0.1\pi$ or 0.9π lead to the steady magneti-

zation $m_x^S = 0$, while $\theta = 0.3\pi, 0.5\pi$ or 0.7π lead to a different steady magnetization $m_x^{\mathcal{P}^+} \neq 0$. Since $m_x^{(N)}(t)$ at arbitrary t goes to the semiclassical limit $m_x(t)$ as $N \rightarrow \infty$, the relaxation time for $\theta = 0.3\pi, 0.5\pi$ or 0.7π must diverge with increasing N . We choose $\theta = 0.8\pi$ (the semiclassical steady magnetization is $m_x^{\mathcal{P}^+}$) to see how the relaxation time increases with N . In fig. 10(b), the black dotted line is $m_x(t)$ in the limit $N \rightarrow \infty$. The curve with $N = 80$ is closer to the black dotted line than the curve with $N = 40$. As a consequence, the curve with $N = 80$ starts to drop much later than the curve with $N = 40$. The relaxation time at $N = 80$ is ten times larger than that at $N = 40$. In fig. 10(c), we choose $\theta = 0.9\pi$ so that $m_x(t)$ at finite N and in the semiclassical limit both relax to zero. Under this initial condition, $m_x^{(N)}(t)$ at finite N goes up and down before it relaxes to zero, and the relaxation time still diverges with increasing N .

In general, one can argue that the relaxation time must diverge in the multistable semiclassical phase. Suppose there are two different semiclassical steady states, called \mathcal{P}_+ and \mathcal{S} without loss of generality. At finite N , the system relaxes to a unique steady state, which may be \mathcal{P}_+ , \mathcal{S} or different from both of them. Let us first suppose that the finite-size system relaxes to \mathcal{P}_+ . Now let us consider the initial condition (θ, ϕ) under which the semiclassical steady state is \mathcal{S} . For an arbitrarily large T , we can find a N so that as the system's size is larger than N it always keeps close to \mathcal{S} for $t < T$. But according to the above assumption, the system has to deviate from \mathcal{S} and relax to \mathcal{P}_+ in the long-time limit. This means that the relaxation time is larger than T . But T can be chosen arbitrarily large. Therefore, the relaxation time must be divergent as N increases. Similarly, we can argue that the relaxation time is divergent if the finite-size system relaxes to \mathcal{S} or some state different from both \mathcal{P}_+ and \mathcal{S} . A divergent relaxation time corresponds to a vanishing Liouvillian gap. We then guess that Δ should be zero within the whole multistable semiclassical phase. This is consistent with what we observe in Sec. IV. The gap certainly vanishes at the DPTs, since the DPTs happen inside the multistable phase.

The real-time dynamics at $p = 3$ or $p = 4$ exhibits similar features as $p = 2$. Fig. 11 plots the transient dynamics of m_x and C_x for $p = 3$ and different values of (κ, h) that are located at the black dots in fig. 1(b). In fig. 11, The black solid lines are $m_x(t)$ and $C_x(t)$ in the semiclassical limit. The parameter pair $(\kappa, h) = (1, -1.6)$ is located in the $\{\mathcal{S}\}$ -phase, in which both $m_x(t)$ and $C_x(t)$ relax towards zero with increasing t (see fig. 11(a) and (b)). While $(\kappa, h) = (1, 1.0)$ is in the $\{\mathcal{P}_-, \mathcal{S}\}$ -phase, and we see that $m_x(t)$ ($C_x(t)$) relaxes towards $m_x^{\mathcal{P}_-}$ ($C_x^{\mathcal{P}_-}$) (see fig. 11(c) and (d)). The blue and red dashed lines are $m_x^{(N)}(t)$ and $C_x^{(N)}(t)$ at finite N . Again, we see that $m_x^{(N)}(t)$ or $C_x^{(N)}(t)$ at small t converge to their semiclassical limits as N increases. But the deviation of blue or red lines from the black solid line is significant at large t ,

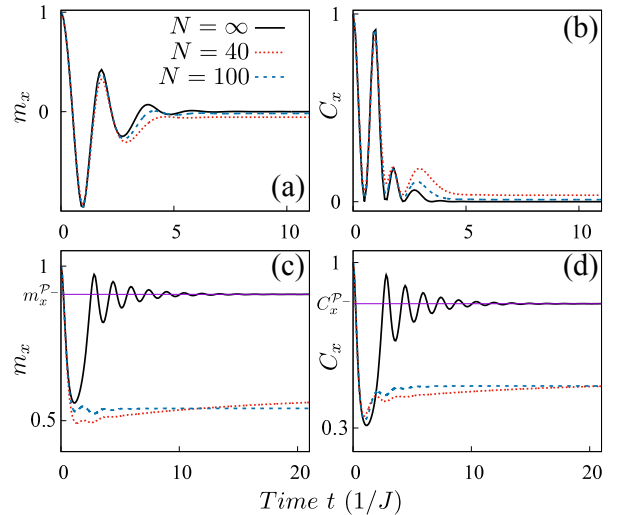


FIG. 11. (Color online) Transient dynamics of m_x and C_x at $p = 3$. Panels (a) and (b) are for $h/J = -1.6$, and (c) and (d) for $h/J = 1.0$. We set $\kappa = J$ and $(\theta, \phi) = (\pi/2, 0)$. All the panels share the same legends. The straight purple lines are $m_x = m_x^{\mathcal{P}_-}$ or $C_x = C_x^{\mathcal{P}_-}$.

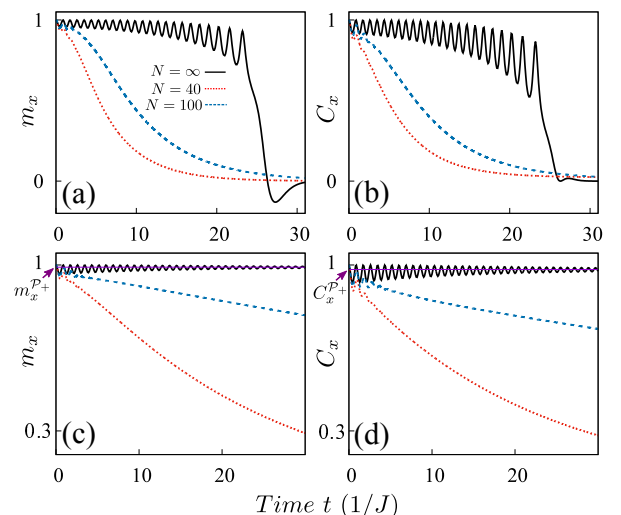


FIG. 12. (Color online) Transient dynamics of m_x and C_x at $p = 4$. Panels (a) and (b) are for $h/J = -0.2$, and (c) and (d) for $h/J = 0.2$. We set $\kappa = J$ and $(\theta, \phi) = (\pi/2, 0)$. All the panels share the same legends. The straight purple lines are $m_x = m_x^{\mathcal{P}_+}$ or $C_x = C_x^{\mathcal{P}_+}$.

at which a larger N is needed for observing the convergence.

Fig. 12 plots the transient dynamics of m_x and C_x for $p = 4$ and different values of (κ, h) that are located at the black dots in fig. 1(c). In the semiclassical limit (black solid line), $m_x(t)$ ($C_x(t)$) relaxes to either zero or $m_x^{\mathcal{P}_+}$ ($C_x^{\mathcal{P}_+}$), depending on the value of h . The red and blue

lines are for $N = 40$ and 100 , respectively. For $h/J = 0.2$ (panels (c) and (d)), the blue or red lines significantly deviate from the semiclassical prediction at large t .

VI. CONCLUSIONS

In this paper we studied a fully-connected p -spin model subject to a collective dissipation and in the presence of a Zeeman field. The model generalizes to generic p , the system studied in references [20] and [28]. The effect of dissipation is to polarize the spins along the z -direction while the interaction between the spins favors the alignment in the x -direction. The competition between the two effects results in a complex phase diagram that depends strongly on the value of p .

In the thermodynamic limit it is possible to derive the steady-state phase diagram through a semi-classical approach. Depending on the value of the couplings different steady states, including \mathcal{S} and \mathcal{P}_\pm , appear as summarized in fig. 1 and table I. Within the semiclassical analysis, multi-stable regions appear, with the steady-state magnetization in thermodynamic limit jumping between that of \mathcal{S} and \mathcal{P}_\pm . The steady state with finite number of spins is unique, being independent of the initial condition. For even values of p , the system has a Z_2 symmetry, which guarantees the magnetization in the x -direction to be zero. For $p \geq 4$, \mathcal{S} and \mathcal{P}_\pm are distinguished from each other in the whole tri-stable region. At the DPTs, the magnetization is discontinuous, jumping between zero (the value in \mathcal{S}) and finite (the value in \mathcal{P}_\pm). The DPTs are first-order. The case $p = 2$ is however special. Except a first-order DPT happens inside

the tri-stable region, there also exists a bistable region in which \mathcal{P}_\pm are stable but \mathcal{S} is not. With increasing Zeeman field, \mathcal{P}_\pm move towards \mathcal{S} . They meet each other at a critical point, where the magnetization variance vanishes continuously, indicating a continuous DPT. On the opposite, when p is odd, the Z_2 symmetry is explicitly broken. First-order DPTs happen inside the bistable region in which both \mathcal{S} and \mathcal{P}_- are stable. The magnetizations in both the x - and z -directions are discontinuous at the DPTs, where they jump between the values in \mathcal{S} and \mathcal{P}_- .

In order to further understand the properties of the transition, we analyzed the finite-scaling properties in the transition regions. To this end, we studied the behavior of the Liouvillian gap as a function of the number of spins. Interesting scaling behavior was found at the continuous DPT, where both the magnetization variance and Liouvillian gap vanish with increasing number of spins according to a power law. On the opposite, the Liouvillian gap was found to vanish exponentially at the first-order DPT.

ACKNOWLEDGEMENT

Pei Wang is supported by NSFC under Grant Nos. 11774315 and 11835011, and by the Junior Associates program of the Abdus Salam International Center for Theoretical Physics. Rosario Fazio acknowledges partial financial support from the Google Quantum Research Award. R. F. research has been conducted within the framework of the Trieste Institute for Theoretical Quantum Technologies (TQT).

* wangpei@zjnu.cn

† On leave

- ¹ A. A. Houck, H. E. Türeci, and J. Koch, Nat. Phys. **8**, 292 (2012).
- ² L. M. Sieberer, M. Buchhold, and S. Diehl, Rep. Prog. Phys. **79**, 096001 (2016).
- ³ M. J. Hartmann, J. Opt. **18**, 104005 (2016).
- ⁴ C. Noh and D. G. Angelakis, Rep. Prog. Phys. **80**, 016401 (2016).
- ⁵ E. Altman, L. M. Sieberer, L. Chen, S. Diehl, and J. Toner, Phys. Rev. X **5**, 011017 (2015).
- ⁶ M. F. Maghrebi and A. V. Gorshkov, Phys. Rev. B **93**, 014307 (2016).
- ⁷ S. Diehl, A. Tomadin, A. Micheli, R. Fazio, and P. Zoller, Phys. Rev. Lett. **105**, 015702 (2010).
- ⁸ R. Rota, F. Minganti, C. Ciuti, and V. Savona, Phys. Rev. Lett. **122**, 110405 (2019).
- ⁹ F. Minganti, A. Biella, N. Bartolo, and C. Ciuti, Phys. Rev. A **98**, 042118 (2018).
- ¹⁰ R. M. Wilson, K. W. Mahmud, A. Hu, A. V. Gorshkov, M. Hafezi, and M. Foss-Feig, Phys. Rev. A **94**, 033801 (2016).
- ¹¹ H. Weimer, Phys. Rev. Lett. **114**, 040402 (2015).
- ¹² A. Kshetrimayum, H. Weimer, and R. Orús, Nat. Commun. **8**, 1291 (2017).
- ¹³ J. Jin, A. Biella, O. Viyuela, C. Ciuti, R. Fazio, and D. Rossini, Phys. Rev. B **98**, 241108 (2018).
- ¹⁴ T. E. Lee, S. Gopalakrishnan, and M. D. Lukin, Phys. Rev. Lett. **110**, 257204 (2013).
- ¹⁵ J. Jin, A. Biella, O. Viyuela, L. Mazza, J. Keeling, R. Fazio, and D. Rossini, Phys. Rev. X **6**, 031011 (2016).
- ¹⁶ A. Biella, J. Jin, O. Viyuela, C. Ciuti, R. Fazio, and D. Rossini, Phys. Rev. B **97**, 035103 (2018).
- ¹⁷ W. Casteels, R. M. Wilson, and M. Wouters, Phys. Rev. A **97**, 062107 (2018).
- ¹⁸ E. M. Kessler, G. Giedke, A. Imamoglu, S. F. Yelin, M. D. Lukin, and J. I. Cirac, Phys. Rev. A **86**, 012116 (2012).
- ¹⁹ W. Casteels, R. Fazio, and C. Ciuti, Phys. Rev. A **95**, 012128 (2017).
- ²⁰ F. Iemini, A. Russomanno, J. Keeling, M. Schiró, M. Dalmonte, and R. Fazio, Phys. Rev. Lett. **121**, 035301 (2018).
- ²¹ B. Bucă, J. Tindall, and D. Jaksch, Nat. Commun. **10**, 1730 (2019).
- ²² C. Lledó, T. K. Mavrogordatos, and M. H. Szymańska, Phys. Rev. B **100**, 054303 (2019).

- ²³ K. Seibold, R. Rota, and V. Savona, *Phys. Rev. A* **101**, 033839 (2020).
- ²⁴ J. O’Sullivan, O. Lunt, C. W. Zollitsch, M. L. W. Thewalt, J. J. L. Morton, and A. Pal, *Dissipative discrete time crystals*, arXiv:1807.09884.
- ²⁵ A. Riera-Campeny, M. Moreno-Cardoner, and A. Sanpera, *Time crystallinity in open quantum systems*, arXiv:1908.11339.
- ²⁶ H. Weimer, A. Kshetrimayum, and R. Orus, *Simulation methods for open quantum many-body systems*, arXiv:1907.07079.
- ²⁷ A. H. Werner, D. Jaschke, P. Silvi, M. Kliesch, T. Calarco, J. Eisert, and S. Montangero, *Phys. Rev. Lett.* **116**, 237201 (2016).
- ²⁸ J. Hannukainen and J. Larson, *Phys. Rev. A* **98**, 042113 (2018).
- ²⁹ K. Tucker, B. Zhu, R. J. Lewis-Swan, J. Marino, F. Jimenez, J. G. Restrepo, and A. M. Rey, *New J. Phys.* **20**, 123003 (2018).
- ³⁰ Z. Gong, R. Hamazaki, and M. Ueda, *Phys. Rev. Lett.* **120**, 040404 (2018).
- ³¹ B. Zhu, J. Marino, N. Y. Yao, M. D. Lukin, and E. A. Demler, *New J. Phys.* **21**, 073028 (2019).
- ³² N. Shammah, S. Ahmed, N. Lambert, S. De Liberato, F. Nori, *Phys. Rev. A* **98**, 063815 (2018).
- ³³ B. Derrida, *Phys. Rev. Lett.* **45**, 79 (1980).
- ³⁴ B. Derrida, *Phys. Rev. B* **24**, 2613 (1981).
- ³⁵ T. Jörg, F. Krzakala, J. Kurchan, A. C. Maggs, and J. Pujos, *EPL* **89**, 40004 (2010).
- ³⁶ V. Bapst and G. Semerjian, *J. Stat. Mech.* **2012**, P06007 (2012).
- ³⁷ B. Seoane and H. Nishimori, *J. Phys. A: Math. Theo.* **45**, 435301 (2012).
- ³⁸ S. Matsuura, H. Nishimori, W. Vinci, T. Albash, and D. A. Lidar, *Phys. Rev. A* **95**, 022308 (2017).
- ³⁹ S. Matsuura, H. Nishimori, W. Vinci, and D. A. Lidar, *Phys. Rev. A* **99**, 062307 (2019).
- ⁴⁰ M. Ohkuwa, H. Nishimori, and D. A. Lidar, *Phys. Rev. A* **98**, 022314 (2018).
- ⁴¹ Y. Susa, Y. Yamashiro, M. Yamamoto, I. Hen, D. A. Lidar, and H. Nishimori, *Phys. Rev. A* **98**, 042326 (2018).
- ⁴² Y. Yamashiro, M. Ohkuwa, H. Nishimori, and D. A. Lidar, *Phys. Rev. A* **100**, 052321 (2019).
- ⁴³ G. Passarelli, G. De Filippis, V. Cataudella, and P. Lucignano, *Phys. Rev. A* **97**, 022319 (2018).
- ⁴⁴ G. Passarelli, V. Cataudella, and P. Lucignano, *Phys. Rev. B* **100**, 024302 (2019).
- ⁴⁵ G. Passarelli, K.-W. Yip, D. A. Lidar, H. Nishimori, and P. Lucignano, *Phys. Rev. A* **101**, 022331 (2020).
- ⁴⁶ G. Passarelli, V. Cataudella, R. Fazio, and P. Lucignano, *Phys. Rev. Research* **2**, 013283 (2020).
- ⁴⁷ L. Del Re, M. Fabrizio, and E. Tosatti, *Phys. Rev. B* **93**, 125131 (2016).
- ⁴⁸ M. M. Wauters, R. Fazio, H. Nishimori, and G. E. Santoro, *Phys. Rev. A* **96**, 022326 (2017).
- ⁴⁹ A. Nava and M. Fabrizio, *Phys. Rev. B* **100**, 125102 (2019).
- ⁵⁰ E. Mpemba and D. Osborne, *Phys. Educ.* **4**, 172 (1969).
- ⁵¹ G. Teschl, *Ordinary Differential Equations and Dynamical Systems* (American Mathematical Society, 2012).
- ⁵² B. Sciolla and G. Biroli, *J. Stat. Mech.* **2011**, P11003 (2011).